RUPTURE PROPAGATION AND FOCUSING OF ENERGY IN A FOAM RUBBER MODEL OF A STICK SLIP EARTHQUAKE

Stephen H. Hartzell

Seismological Laboratory, California Institute of Technology
Pasadena, California 91125

Ralph J. Archuleta

U.S. Geological Survey, Menlo Park, California 94025

Abstract. Dynamic displacements and velocities measured at the surface of a block of foam rubber are analyzed for stick slip events on faults with three different geometries; elliptical, rectangular (aspect ratio of 3.33), and long thin (aspect ratio of 12.66). Over 100 separate events were recorded, each with up to eight simultaneous point measurements of particle displacement. The positions of the measurements were along the fault trace and to distances of a few fault lengths. Acceleration of the rupture front is observed as the rupture propagates out from its point of nucleation. Deceleration of the rupture is also observed when it enters a region of lower effective stress. In the direction of rupture propagation the static displacements along the fault trace increase, and the rise times decrease. The combined effect causes a rapid increase in particle velocities. For a predominantly unilateral rupture, increases in particle velocities by a factor of 2 or 3 over those recorded near the center of the fault trace are common. At higher rupture velocities, there is a larger increase in the particle velocity (or decrease in the rise time) for a given increase in the static displacement. The amplitude of the far-field displacement is similarly strongly dependent on the nature of the rupture. Differences in far-field displacements of an order of magnitude are seen for measurements at equal distances from a unilateral rupture. When the rupture initiates at depth, a much more uniform distribution of particle displacements and velocities is obtained. Afterslip, i.e., motion occurring significantly slower than the time required for a shear wave to travel the length of the fault, is also observed. Comparison of our model results with surface static displacements following major earthquakes suggests that observed variation in static displacements may be due in part to variations in the bedrock stress field. Such stress heterogeneity can lead to a division of a major earthquake into a series of several subruptures, each of which rupture coherently, but the event as a whole behaves incoherently.

Introduction

Brune [1973] first studied stick slip events in foam rubber. Stick slip along precut fault surfaces in stressed foam rubber was shown to have many of the characteristics of earthquake slip along faults in the earth. The peak particle velocities near the center of the fault were about half the value $\Delta\sigma\beta/\mu$, with $\Delta\sigma\beta/\mu$ apparently being a good upper bound. Here $\Delta\sigma$ is the stress drop, β the shear wave velocity, and μ the rigidity. This initial study was limited to the measurement of slip at a single location on the fault, for each event. Thus rupture propagation effects could only be inferred. Later Archuleta and Brune [1975] used high-speed photography to record the time history of displacement at many different points simultaneously, both on and off the fault. The distribution of static displacements for a circular fault model agreed well with the theoretical value of Keilis-Borok [1959] and Neuber [1937]. An apparent rupture velocity of 0.7β was measured, which coincidentally is consistent with observations of rupture velocity for actual earthquakes [Geller, 1976]. Perhaps the most interesting result was the observation of the shortening of the rise time on the fault in the direction of rupture propagation. Generally good agreement was obtained between the dynamic displacements on the fault and the analytical results for an expanding circular fault [Richards, 1973] as well as results from a two-dimensional numerical model [Hanson *et al.*, 1974]. High-frequency resolution of the slip functions was limited because of constraints imposed by both the photographic process and the digitization of the film. In this paper, multiple simultaneous point measurements of particle displacement are made using a technique that greatly improves the resolution over the previous model studies. For the first time, 'far-field' displacements (at distances of a few fault lengths) are measured and interpreted in terms of the rupture history on the fault plane. The data show realistic dynamic faulting, with acceleration and deceleration of the rupture front, as well as variations in the static displacement field. Focusing of energy due to a coherently propagating rupture is evident. (The term focusing in this paper is used with analogy to the focusing of energy by an antenna array rather than the converging of a ray bundle by a lens.) However, small-scale variations in the displacement and velocity field are also present, which tend to disrupt the coherency and which are probably present during faulting in the earth. Such incoherent ruptures are richer in high frequencies.

These observations of model experiments yield qualitative insight into the faulting process occurring in an actual earthquake and the distribution of the ground motion likely to accompany a major earthquake. The experiments

Paper number 9B0221.
0148-0227/79/009B-0221$01.00

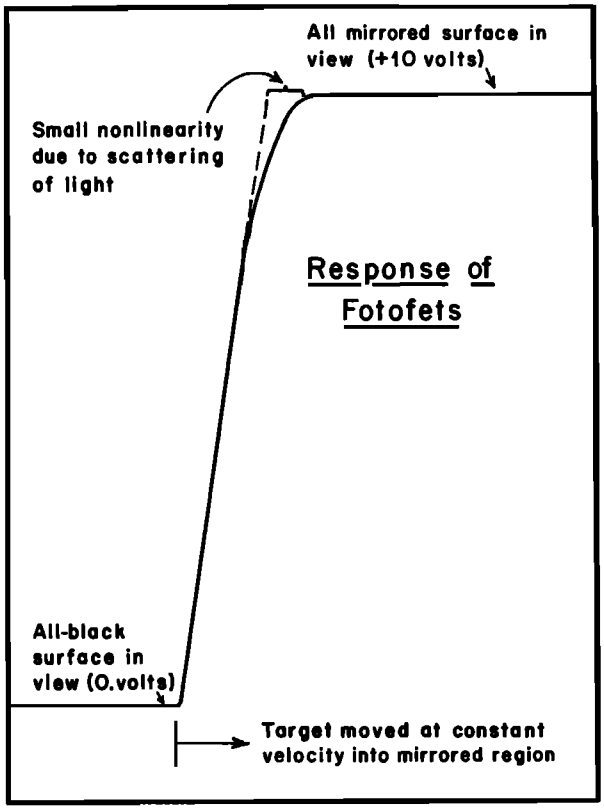

Fig. 1. Response of light sensitive Fotofets used to record surface displacements in the foam rubber.

in foam rubber were designed to illuminate our understanding of the pattern of particle motion caused by a propagating stress relaxation. Quantitative scaling to faulting in the earth requires a knowledge of the frictional properties of foam rubber, which is beyond the scope of this study.

Experimental Procedure

The homogeneous, isotropic, elastic medium in our model is a block of polyurethene elastomer (foam rubber), with dimensions 76 cm x 76 cm x 38 cm. The voids in the foam rubber are less than 1 mm in diameter, significantly less than the shortest wavelength λ, which contributes to the measurements of displacement. The foam blocks therefore are a very good approximation to a homogeneous half space. A slip plane of desired geometery is cut into the surface of the foam block, representing a preexisting fault. Uniform normal and shear stresses are applied, resulting in stick slip events on the fault surface. The mechanical apparatus used to apply uniform normal and shear stress to the foam rubber blocks has been discussed in detail by Brune [1973] and Archuleta and Brune [1975]. In this study the strains are typically of the order of 10^{-2}, compared with earthquakes where strains are typically of the order of 10^{-4}. Despite these relatively large strains the foam rubber appears to behave linearly.

The high quality of the data presented in this study is a result of a new recording system. The system utilizes a light sensitive field effect transistor (Fotofet, FF409, Teledyne Crystallonics) and an analog-to-digital recorder. As many as eight points are selected at which the displacement time history is to be measured. These points may lie in either the near field or the far field of the model rupture. At these points, thin, lightweight, rectangular (10 mm x 5 mm) glass slide covers, or 'targets', are securely attached. Half of each target is painted flat black, while the other half is a mirrored surface. Above each target (about 10 mm), and decoupled from the rest of the experimental apparatus, are two cylindrical tubes, both of which are directed toward the target. In one tube is a uniform light source powered by direct current to minimize noise. The other tube is a collimator and a Fotofet, which is centered on the dividing line between mirrored surface and black surface. Very small horizontal movements of the target produce variations in the amount of light which reaches the Fotofet. The Fotofet in turn produces an analog voltage signal which is passed through a preamp and then an amplifier. The response of a representative Fotofet is shown in Figure 1. The output voltage from the Fotofet is plotted for the case where the target is made to move at a constant velocity from the all-black position (0. V) to the all-mirrored position (+10. V). The response is linear over almost its entire length, with only a small nonlinearity due to scattering of light near the all-mirrored position. Since targets are operated near the all-black position, this small nonlinearity has no measurable effect on our results.

The amplified signal is fed to a Biomation Transient Recorder model 1015. The transient recorder converts the voltage signal to a string of 1024 10-bit words at a sample interval of 0.2 ms. The total recording time per event is thus 204.8 ms. The transient recorder has a built-in delay line which ensures the recording of the initial part of the triggering event. The output from the transient recorder is written to magnetic tape for future analysis.

In order to make many simultaneous measurements, two transient recorders are used, each having four input channels. Each channel records the output from a different Fotofet sensor. The system is set up such that one Fotofet serves as the master trigger for the other seven. Because of the built-in delay line for each channel of the transient recorder, the full recording of each event on all eight recorders is guaranteed. Overall, more than 500 digitized particle displacement time histories were obtained.

Three different fault geometries are studied. An elliptical fault, which was also used in the original Brune [1973] study, a rectangular fault, and a long thin fault. All three faults are

TABLE 1. Model Fault Parameters

Fault	Length, cm	Width, cm	β, cm/s
Elliptical	24.3	5.7	3700
Rectangular	20.0	6.0	5800
Long	76.0	6.0	5800

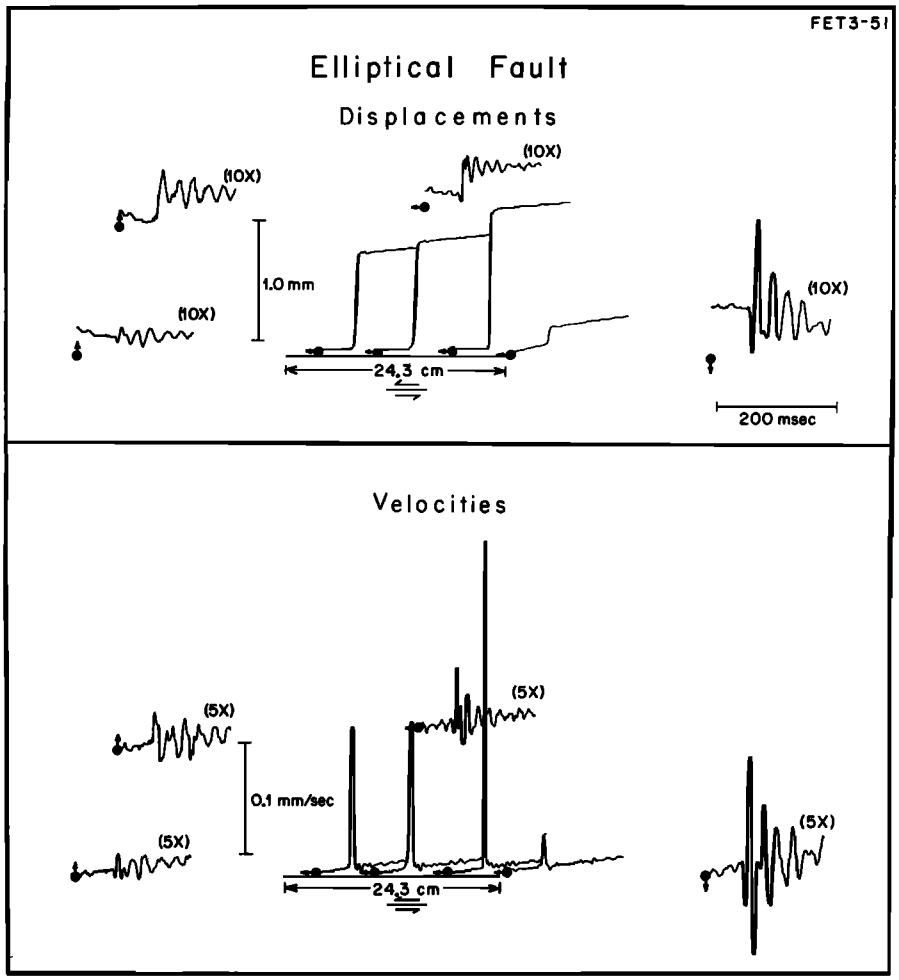

Fig. 2. A nearly unilateral rupture to the right on the elliptical fault.

vertical. The corresponding fault dimensions and shear wave velocities of the foam blocks are given in Table 1. The long fault runs the entire length of the foam block and suggests the nature in which an earthquake rupture may stop when it does not run into a preexisting fault boundary but rather dies out in a region of higher fractional stress.

Just over 100 separate events are recorded for the above three fault models, with up to eight simultaneous measurements of dynamic displacement each. The targets are oriented so that we measure either the component of displacement parallel to the fault trace or perpendicular (transverse) to the fault trace. The displacement record is numerically differentiated to obtain velocity. At least three measurements of displacement are always made along the trace of the fault. This procedure allows us to determine if the rupture is bilateral or unilateral and to get some idea of the rupture velocity. With more than three observation points on the fault, a better estimate of the rupture velocity is obtained. The time of the peak particle velocity is taken as the arrival time of the rupture front. The rupture velocity estimated in the above manner is actually the apparent rupture velocity along the surface. If the rupture is initiated at depth, the rupture velocity at depth is less than the apparent rupture velocity at the surface. The remaining target-Fotofet combinations are distributed at greater distances from the fault. We refer to the measurements at distances of a few fault lengths as 'far-field' measurements. Strictly speaking, this is not correct, since the epicentral distances are not large in comparison to the source dimension and many of the displacement records still have measurable static offsets. However, these records display much of the character of true far-field recordings, and as such it is convenient to refer to them as far-field recordings.

Results

Figures 2, 3, and 6-13 are a representative selection of 10 different events from the elliptical, rectangular, and long faults. Each is given a number, prefixed by the letters FET, in the upper right-hand corner. In the rest of the paper we shall refer to individual events by these numbers. Each of the 10 figures shows the recorded displacements in the upper half of the figure. Numbers in parentheses, such as (10x), are scaling factors by which the associated displacement or velocity has been multiplied. At the beginning of each time history, there is a large dot and arrow, which indicate the position of the target and the direction of positive motion, respectively. The trace of the fault is shown as a straight line and labeled as to the sense of the motion, that is, left lateral or

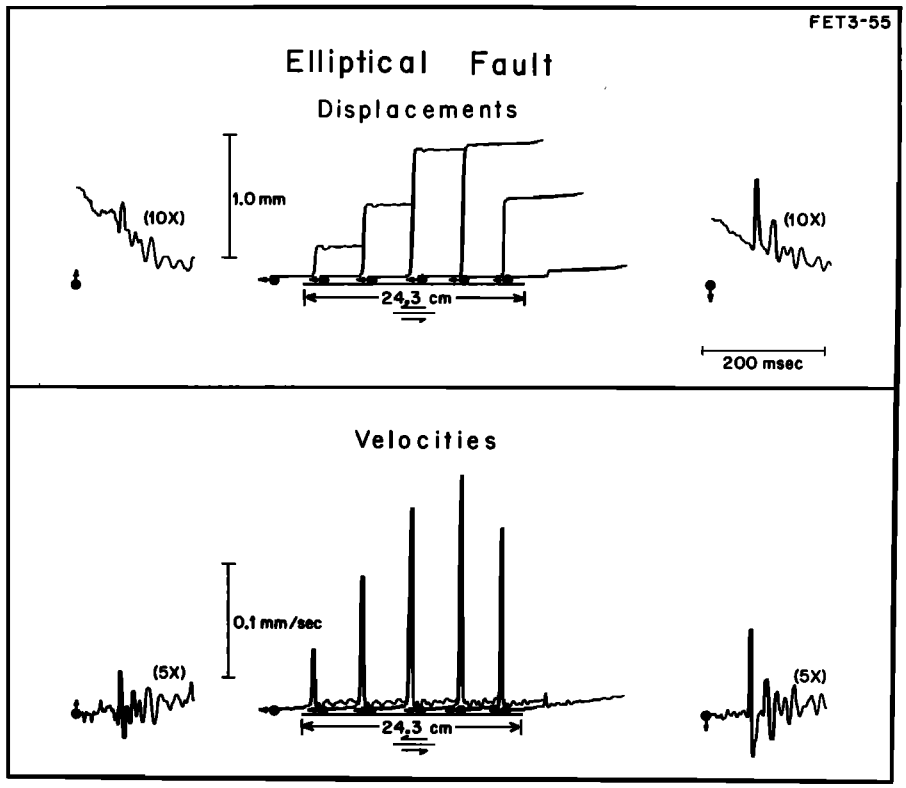

Fig. 3. A nearly bilateral rupture on the elliptical fault.

right lateral. For each figure the position of the targets relative to the fault has been drawn to scale using the given fault length as the scale. The total time of each displacement and velocity record is 200 ms.

Before considering some of the events in greater detail we first note the general features of the records. Along the trace of the fault the parallel displacements are close to zero until the arrival of the rupture front. The slowly

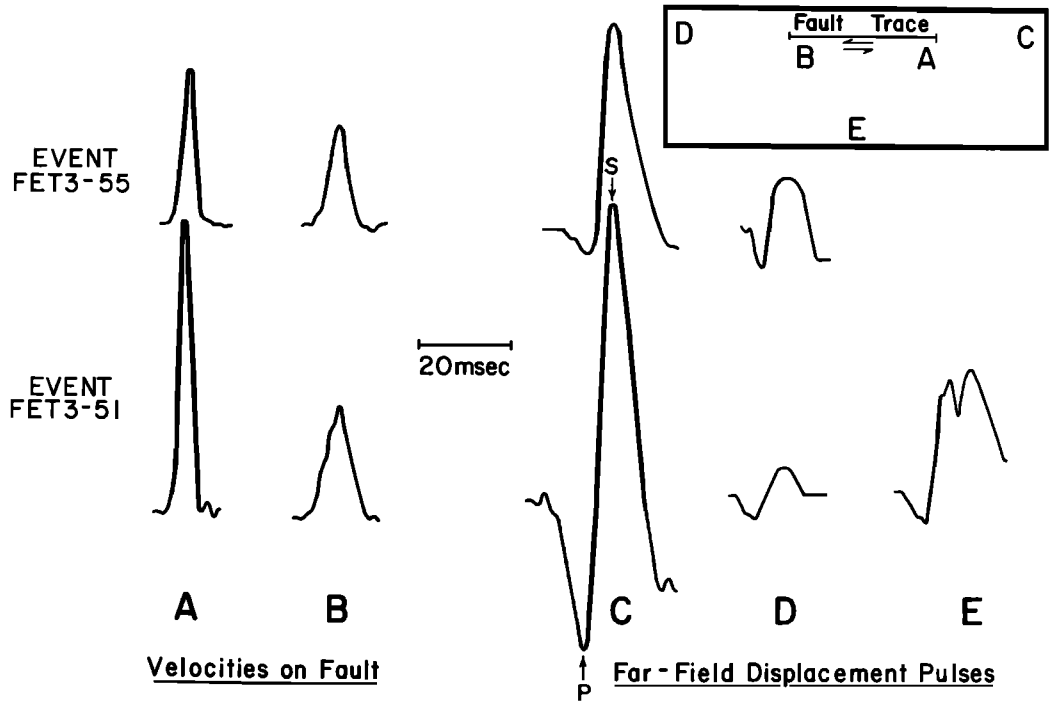

Fig. 4. Details of particle velocities on the fault trace and the corresponding far-field displacements for the two events on the elliptical fault pictured in Figures 2 and 3.

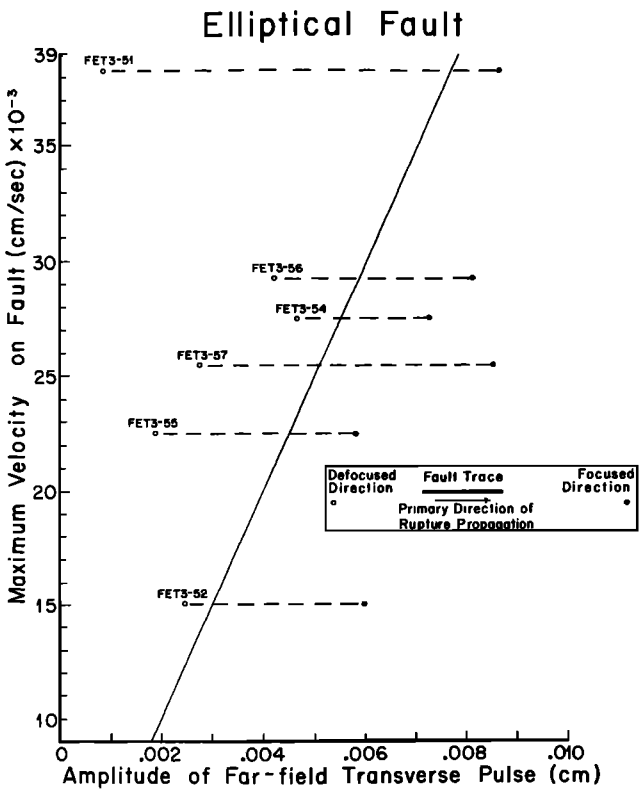

Fig. 5. Plot of the maximum particle velocity on the elliptical fault versus the amplitude of the far-field transverse pulse in the focused and defocused directions for six separate events. The focused direction is defined to be the primary direction of rupture propagation, and the defocused direction is 180° from the focused direction. In each case the focused and defocused amplitudes are measured at very nearly the same distance from the fault.

increasing initial displacement seen in some figures is related to triggering the rupture rather than being caused by the rupture. When the rupture front arrives, the displacement rapidly changes to its static value, producing a velocity pulse. The magnitude of the static offset, as well as the details of how the displacement proceeds to its final value, is a function of both the fault geometry and the nature of the growth of the rupture front. As one moves away from the fault, the static offset decreases and, as expected, develops a pulselike character. Some of the far-field records have an oscillatory character following the first arrival. These oscillations are due to repeated reflections from the sides of the foam block. Some long-period noise is also more evident in the far-field displacements and is a result of the lower signal to noise ratio at these distances.

Figure 4 is a comparison between the particle velocities on the fault and the far-field displacements for the two events shown in Figures 2 and 3 (FET3-51 and FET3-55). The inset in Figure 4 shows roughly where the measurements of velocity and displacement were made in relation to the fault. For the exact location and orientation of the targets, one should refer to Figures 2 and 3. All velocities and displacements are plotted on the same two scales for relative comparison. We define $G_i(\underset{\sim}{x},t;\underset{\sim}{x}',t')$ to be the displacement in the i direction at $(\underset{\sim}{x},t)$ due to a point shear dislocation at $\underset{\sim}{x}'$ applied as a unit step function at t'. By the representation theorem of Volterra the displacement $U_i(\underset{\sim}{x},t)$ in the i direction for a fault surface Σ may be written as

$$U_i(\underset{\sim}{x},t) = \int_{\Sigma} dA \int_{-\infty}^{\infty} dt' G_i(\underset{\sim}{x},t;\underset{\sim}{x}',t') \Delta\dot{s}(\underset{\sim}{x}',t')$$

where $\Delta\dot{s}(\underset{\sim}{x}',t')$ is the slip velocity function on the fault surface. Since the particle velocities in Figure 4 are measured close to the slip plane, $\Delta\dot{s}(\underset{\sim}{x}',t')$ can be reasonably approximated by 2 times the measured particle velocity. The above relationship between $U_i(\underset{\sim}{x},t)$ and $\Delta\dot{s}(\underset{\sim}{x}',t')$ is borne out in our measurements by noting the similarity between the velocity functions and their corresponding far-field displacements in Figure 4. We will have occasion to refer to Figure 4 in the following more detailed analysis of selected events.

Elliptical Fault

FET3-51 (Figure 2) represents a nearly unilateral rupture to the right. As mentioned

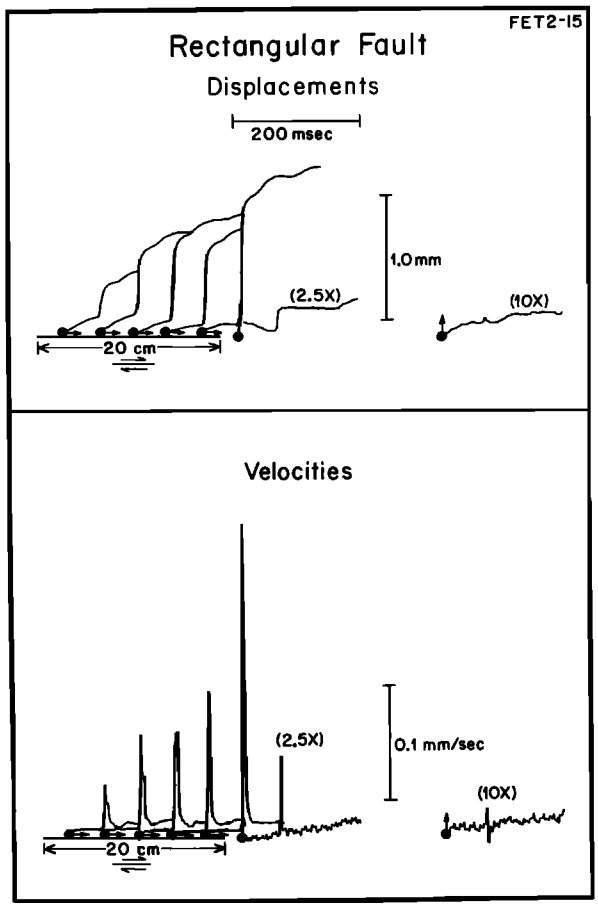

Fig. 6. A unilateral rupture to the right on the rectangular fault, showing acceleration of the rupture front.

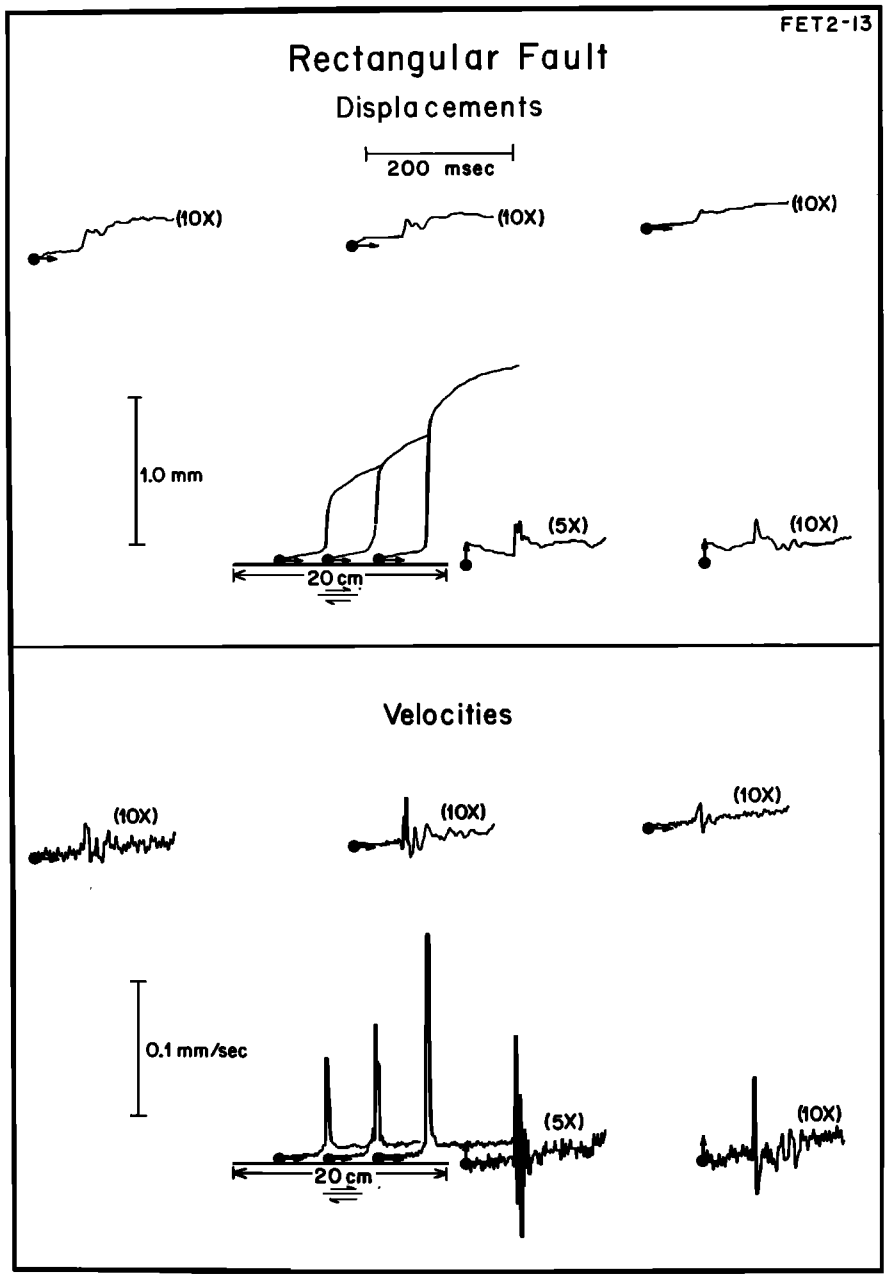

Fig. 7. Comparison of near-field and far-field displacements and velocities for the rectangular fault.

above, the time corresponding to the peak particle velocity is taken as the arrival time of the rupture front. Using the relative time difference between targets, the average apparent rupture velocity is estimated to be very nearly equal to β. A propagating rupture has several effects on the particle motion. Although the static displacements show a general increase in the direction of rupture propagation, the dramatic effect of the rupture is the increase in amplitude of the particle velocity. Both a shortening of the rise time and an increase in the static displacements along the fault produce particle velocities that are a factor of 2 larger at the right end of the fault. These effects due to rupture propagation are significant when considering the problem of estimating maximum particle velocity and acceleration in the near field. It is interesting to note that the static displacements along the fault in Figure 2 differ from the elliptical displacement field predicted by static theory [Eshelby, 1957], whereas there is general agreement with the theory for event FET3-55 (Figure 3), which is closer to a bilateral rupture. Referring to Figure 4, the propagating rupture produces dramatically larger far-field displacements in the direction of rupture propagation (by about an order of magnitude) in comparison to the direction opposite that of propagation. The size of the far-field displacement perpendicular to the trace of the fault lies between the two above extremes. Similar results have been computed by Hartzell *et al.* [1978] for finite, kinematic fault models in a homogeneous half space. The far-field

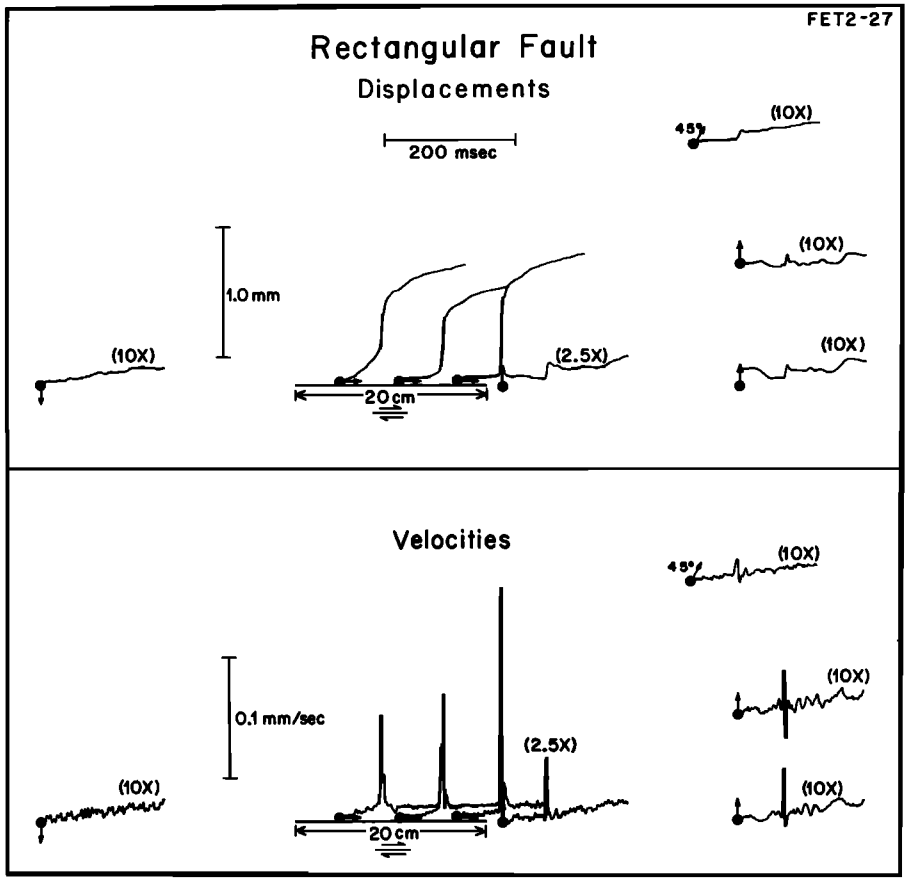

Fig. 8. Comparison of near-field and far-field displacements and velocities for the rectangular fault.

displacement pulse in the focused direction also shows a very clearly recorded near-field P term (arriving early and opposite in motion to the S wave), indicated in Figure 4.

FET3-55 (Figure 3) is similar to FET3-51 (Figure 2), except that the rupture is initiated more closely to the center of the fault and spreads out bilaterally. As a result the focusing to the right is not quite as strong, being a more nearly symmetric rupture. Similar focusing effects are seen in the far-field (Figure 4) for FET3-55 as for FET3-51, but the effects are not as large. The static displacements have the general elliptical shape as a function of position along the fault as expected from static theory [Eshelby, 1957].

The effect of rupture propagation on far-field displacements, for the elliptical fault, are summarized in Figure 5. The maximum measured particle velocity on the fault is plotted against the amplitude of the far-field transverse pulse (motion normal to trace of fault) in both the focused and defocused directions. The focused direction is defined to be along the strike of the fault in the primary direction of rupture propagation. That is, none of the events are perfect bilateral ruptures. The defocused direction is 180° from the focused direction. Amplitudes are plotted for six separate events, with a dotted line connecting focused and defocused amplitudes for the same event. In each case, focused and defocused amplitudes are measured at very nearly the same distance from the fault. A linear relationship is expected between the amplitude of the far-field displacement and the maximum particle velocity on the fault. The solid line in Figure 5 shows a simple linear trade-off between peak velocity on the fault and far-field amplitudes and is included as a reference line. We see that in general, larger particle velocities on the fault lead to larger far-field amplitudes, in both the focused and the defocused directions. However, the details of the rupture propagation can modify this trend significantly. The displacements in the focused direction are always greater than the displacements in the defocused direction. However, a predominantly unilateral rupture with a rupture velocity close to β, such as FET3-51, produces a larger spread between the focused and defocused amplitudes than one with a lower rupture velocity or one which is more nearly bilateral.

Rectangular Fault

Four events are illustrated for the rectangular fault: FET2-15 (Figure 6), FET2-13 (Figure 7), FET2-27 (Figure 8), and FET2-37 (Figure 9). One obvious difference between the rectangular fault (and to some extent the long fault discussed below) and the elliptical fault is in the nature of the displacements on the fault. The displacements on the elliptical fault are very much like simple ramps, with sharp onsets and equally sharp terminations, whereas the displacements on the rectangular fault have sharp onsets but much more gradual terminations, as

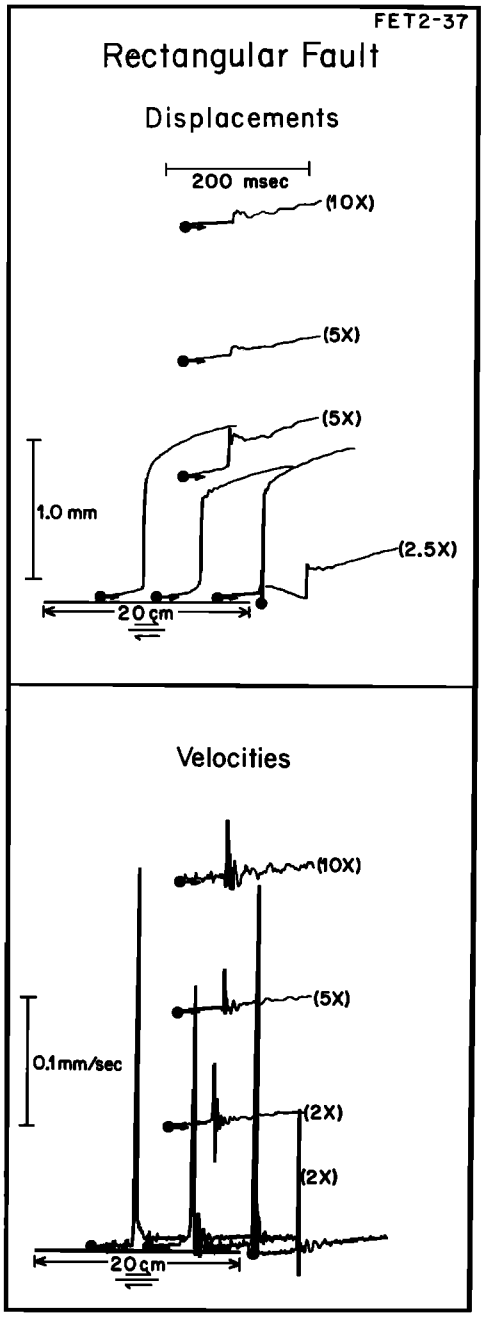

Fig. 9. Rupture initiation at depth on the rectangular fault with an apparent rupture velocity at the surface of greater than β, resulting in a more uniform distribution of displacements and velocities.

they approach their static values. The rectangular fault seems to be characterized by a two-stage rupture mechanism: (1) an initial sharp displacement with rise time approximately equal to the time required for a shear wave to travel the length of the fault, followed by (2) a much slower afterslip process, resulting in slip on the already established fault plane. It is this second stage which distinguishes the rectangular fault from the elliptical fault discussed above and which may be due to the different material properties of the foam rubber used in the rectangular fault model (see Table 1). Such an afterslip process has been postulated in several recent earthquake studies as a possible explanation for the larger estimates of moment based on distant surface waves, compared with moment estimates based on local body waves [Kanamori, 1973; Hartzell and Brune, 1977].

FET2-15 (Figure 6) appears to be a nearly complete unilateral rupture, commencing at the far left end of the fault and propagating to the right. Relative times between adjacent targets indicate an acceleration of the rupture front, from 0.7β near its point of initiation to 0.9β at the other end of the fault. Acceleration of the rupture front may account for the nonlinear increase in particle velocities along the fault. We shall discuss this point further below.

FET2-37 (Figure 9) has an apparent rupture velocity along the surface of greater than β. This suggests that the rupture commenced at depth and propagated primarily upward. Such a rupture is characterized by much more uniform particle velocities along the fault than for a rupture which nucleates near the surface (compare velocities with FET2-15, Figure 6 above). This result is also consistent with the dynamic stress relaxation models of Archuleta and Frazier [1978]. The arrangement of targets perpendicular to the trace of the fault in Figure 9 affords a reasonably accurate estimate of β. The targets are positioned along a maximum in the shear wave radiation pattern. The obvious positive step in displacement seen in these records is the shear wave propagating out from the fault. The value of β estimated from this event and similar events is 5800 cm/s (Table 1). Hartzell *et al.* [1978], using a finite kinematic fault model, obtain a reasonable fit to the displacement records for an event very similar to FET2-37 (Figure 9). Such fits indicate that the foam rubber model can be used to predict the character of strong ground motion within a few fault lengths.

FET2-13 (Figure 7) and FET2-27 (Figure 8) illustrate the character of the far-field particle displacements and velocities for the rectangular fault. Note the asymmetry in far-field amplitudes in Figure 8 (off left end compared to off right end of fault) caused by a propagating rupture to the right.

Long Fault

The final four events are for the long fault: FET3-63 (Figure 10), FET3-70 (Figure 11), FET3-87 (Figure 12), and FET3-92 (Figure 13). The long fault is cut the entire length of the foam block to a depth of 6 cm and is meant to model slip over a surface which does not have well defined, preexisting boundaries. With such a model we may study the decay of the slip function as the rupture propagates into a region of lower effective stress and is brought to a stop by frictional forces. In our model we purposely initiate the rupture near the right end of the long fault by locally reducing the normal stress. To the left the rupture propagates into a region of higher normal stress and thus higher frictional stress and comes to a gradual stop. The apparent rupture velocity decreases from a value near β in the region where the static displacements are the largest (between the third and fourth targets from the right) to

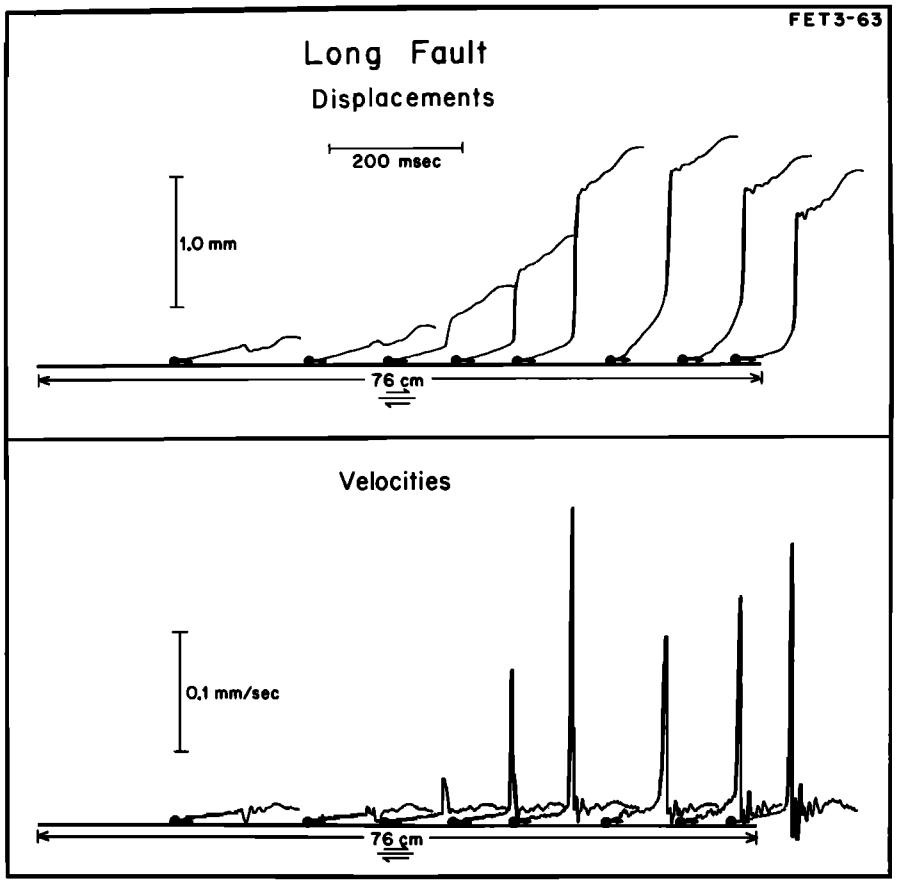

Fig. 10. A bilateral rupture on the long fault. The rupture decelerates and dies out to the left in a region of lower effective stress.

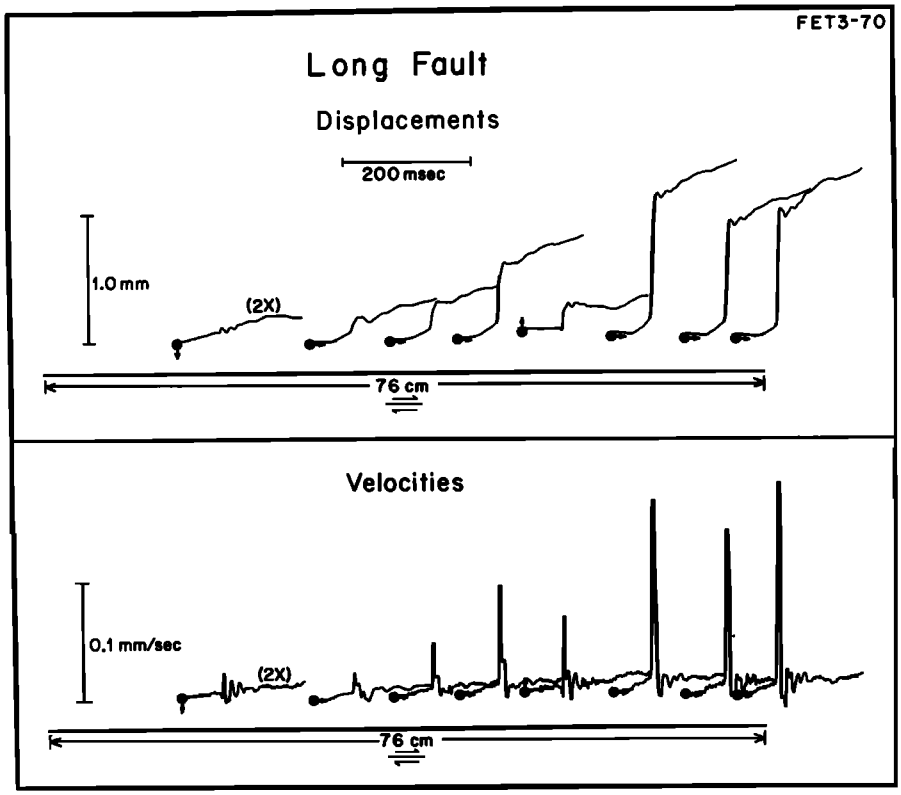

Fig. 11. Displacements and velocities a short distance off the fault for an event on the long fault similar to the one pictured in Figure 10.

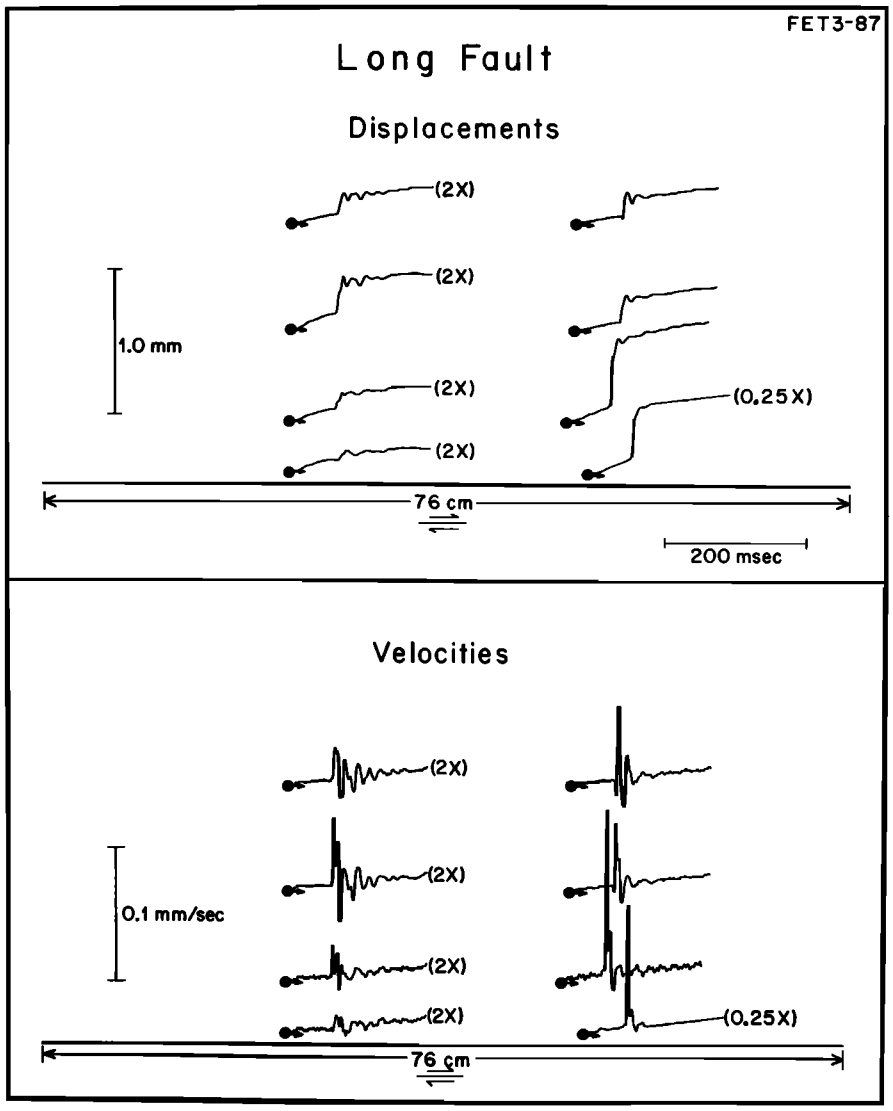

Fig. 12. Decay of displacements and velocities parallel to the long fault.

≈0.5β near the left end of the fault. Measurements of rupture velocity at the extreme left end of the fault are not possible owing to the nonimpulsive nature of the displacements. To the right the rupture breaks out at the free surface at the end of the foam block.

There is a high degree of reproducibility in the long fault events. Each of the four events illustrated has quite similar rupture histories and static displacements on the fault. We can therefore view Figures 10 through 13 as 32 point measurements of displacement and velocity for a single event, without significant error. From Figures 10 and 11 we see that the slip on the fault slowly dies out as the rupture propagates into the region of higher normal (frictional) stress. The displacement normal to the fault (the fourth trace from the right in Figure 11) is about a factor of 6 less than the maximum displacement parallel to the fault. This agrees quite well with the theoretical value for the normal displacement [Neuber, 1937; Eshelby, 1957]. The normal particle velocity is, however, only about a factor of 2 less than the parallel particle velocity. Figures 12 and 13 both have two lines of targets, going out normal to the fault, each line coming off at a different location along the fault. Examining the leftmost line of targets in each figure, we see that the targets further from the fault experience greater displacements and velocities than the targets closer to the fault. This may seem like an unusual result until one realizes that the major slip on the fault takes place to the right of where the line of targets takes off from the fault trace. The targets further from the fault therefore lie in a region of a maximum in the P wave radiation pattern.

The variation in slip along the trace of the long fault (Figures 10 and 11) has a more random character than for the elliptical or rectangular faults. The variation is attributed to heterogeneity of stress drop and is discussed in the final section on comparison with slip during earthquakes.

Particle Velocities

Brune [1970], by considering a simple rupture model, obtained $\sigma\beta/\mu$ as an estimate of the

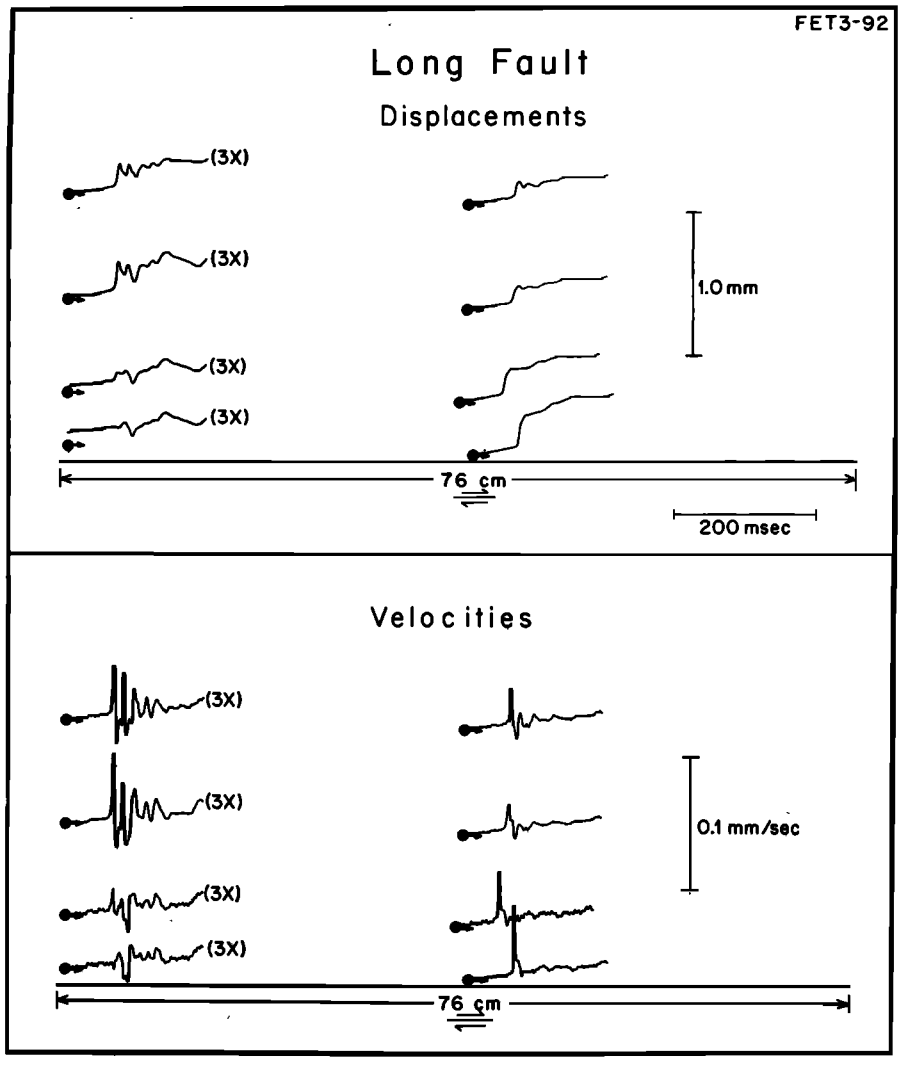

Fig. 13. Decay of displacements and velocities parallel to the long fault.

particle velocity on the fault, where σ is the effective stress, or the stress above the frictional stress available to drive the fault. Kanamori [1972] later used the above expression to estimate the effective stress acting during shallow strike slip faulting in Japan. Brune [1973], using a foam rubber model of a dynamic rupture, found that the peak particle velocity near the center of the fault, $\dot{U}_{max}$, averaged about half the value $\Delta\sigma\beta/\mu$, with $\Delta\sigma\beta/\mu$ being a good upper bound (for the case where the effective stress is equal to the stress drop $\Delta\sigma$). Similar results are obtained in this study. We use the Knopoff [1958] expression for the stress drop on a long thin fault,

$$\Delta\sigma = \frac{\mu}{2}\frac{u_{max}}{w}$$

where u_{max} is the maximum dislocation on the fault and w is the fault width. The maximum particle velocity on the fault, in terms of the displacement of one side of the fault, U_{max} (which is the quantity measured in our model experiments) is then

$$\dot{U}_{max} = \frac{\beta U_{max}}{w}$$

For the rectangular fault and long fault the above expression becomes $\dot{U}_{max} = (966/s)\, U_{max}$. For the elliptical fault we have $\dot{U}_{max} = (649/s)U_{max}$. These are only approximations, since the fault models in this study have finite lengths. Static displacements on the fault and the associated peak particle velocities for the three fault types are plotted in Figure 14. For clarity, only a few events are considered. Individual measurements are plotted as small dots. Values for adjacent targets on the fault, for a given event, are connected with line segments. Some of the more reliable estimates of apparent rupture velocity (ranging from 0.5β to greater than β) between adjacent targets are also indicated. There is a general trend for steeper slopes as the rupture velocity increases. That is, for higher rupture velocities, there is a greater increase in the particle velocity (or decrease in the rise time) for a given increase in the static displacement.

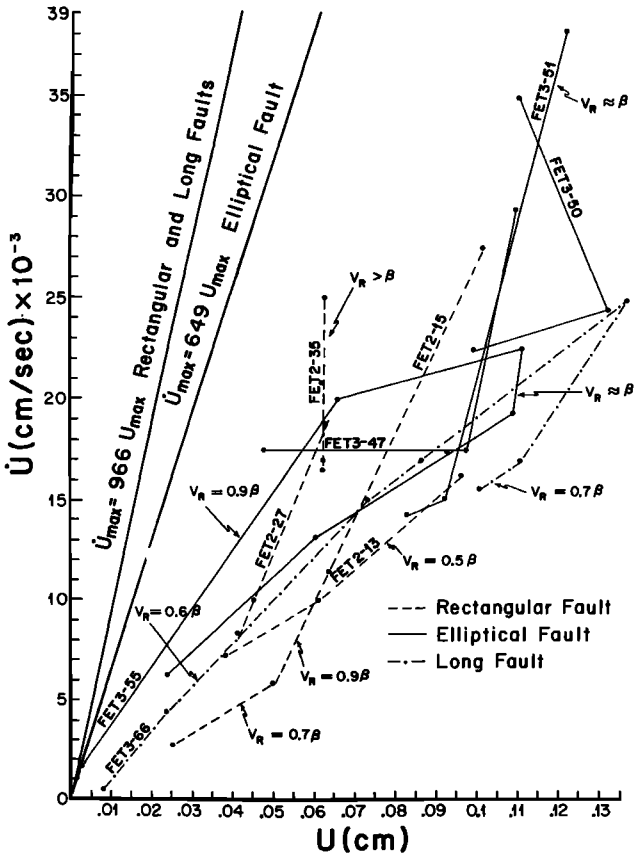

Fig. 14. Plot of the particle velocity versus the static displacement on the fault for a few events from the three fault geometries studied. Individual measurements are indicated by small dots. Adjacent measurements along the fault trace for a given event are joined by line segments. Some of the more reliable measurements of apparent rupture velocity between targets are indicated. The heavy straight lines are estimates of the theoretical maximum particle velocity on the fault (see text).

Comparison with Slip During Earthquakes

An important characteristic of measured surface ground displacement after moderate to large earthquakes is its apparent irregularity along the fault trace. Several examples are given in Figure 15: 1974 strike slip earthquake in Japan [Matsuda and Yamashina, 1974]; 1968 Borrego Mountain, California, earthquake [Clark, 1972]; and 1976 Guatemalan earthquake [Bucknam *et al.*, 1978]. Errors in measurement can cause some of the variability but in most cases only a small percentage. A greater proportion of the irregularity in static offsets can probably be attributed to lower-rigidity surface layers, whose offsets do not always accurately reflect the displacements in the basement rock. Such decoupling between basement rock and surface sediments may be the explanation for afterslip on faults which break the free surface. Afterslip on a fault following an earthquake has been observed for several earthquakes, in particular, the 1968 Borrego Mountain earthquake [Burford, 1972] and the 1966 Parkfield earthquake [Smith and Wyss, 1968]. In general, greater amounts of afterslip are associated with the fault segments which show the least amount of offset immediately following the earthquake. The afterslip process therefore has a tendency toward smoothing out the long-term, surface static offsets. However, even with the above considerations, there seems to be too much variability in static offsets. It seems plausible that a certain percentage of the irregularity in surface displacements reflects true randomness in the displacements in the basement rock.

Most theoretical and numerical solutions of stress relaxation problems do not predict the observed randomness in displacement, because they are constrained to satisfy uniform stress and/or rupture propagation velocity requirements. In modeling the earth these constraints are obviously unrealistic but usually must be assumed to make the problem tractable. In the foam rubber experiment the equipment is designed to apply 'uniform' normal and shear stress to the foam blocks, but this is obviously an approximation. Small irregularities in the fault surface are also introduced owing to our inability to make perfectly smooth, planar cuts in the foam. These imperfections result in a heterogeneous frictional stress field [Nur, 1977], which in turn imparts a certain amount of randomness to the static offsets and particle velocities on the fault. Effects of this kind are most clearly seen in the long fault model, where stress heterogeneities are more likely to be present (for example, Figure 10). The foam rubber model is used as an approximation to a homogeneous half space with uniform stresses, but it still shows some randomness in the displacements and particle velocities. The earth is probably not as uniform as our laboratory model. The random character of the displacements in Figure 15 is therefore not surprising.

The wavelength of the irregularities in Figure 15 may be related to the coherence length of the rupture. The foam rubber model does produce smoothly varying displacements and particle velocities (i.e., less random behavior) over shorter lengths (see Figure 3). Such features indicate a smoothly propagating (coherent) rupture. The static displacements for the Guatemalan earthquake show a very uniform region between 105 km and 155 km [Bucknam *et al.*, 1978]. This section of the fault may represent a single, well-defined, coherent rupture. The fault over its entire length, however, behaves incoherently [Kanamori and Stewart, 1978]. Coherent rupture propagation causes destructive interference at high frequencies [Boore and Joyner 1978]. A coherent rupture over a given fault length will produce large displacements in the focused direction, as exhibited in the foam rubber model. However, an incoherent rupture over the same fault length is likely to produce similar displacements but significantly higher velocities and much higher accelerations. Most mathematical models of earthquakes have not considered coherence lengths in rupture propagation and therefore may underestimate the amount of high-frequency energy.

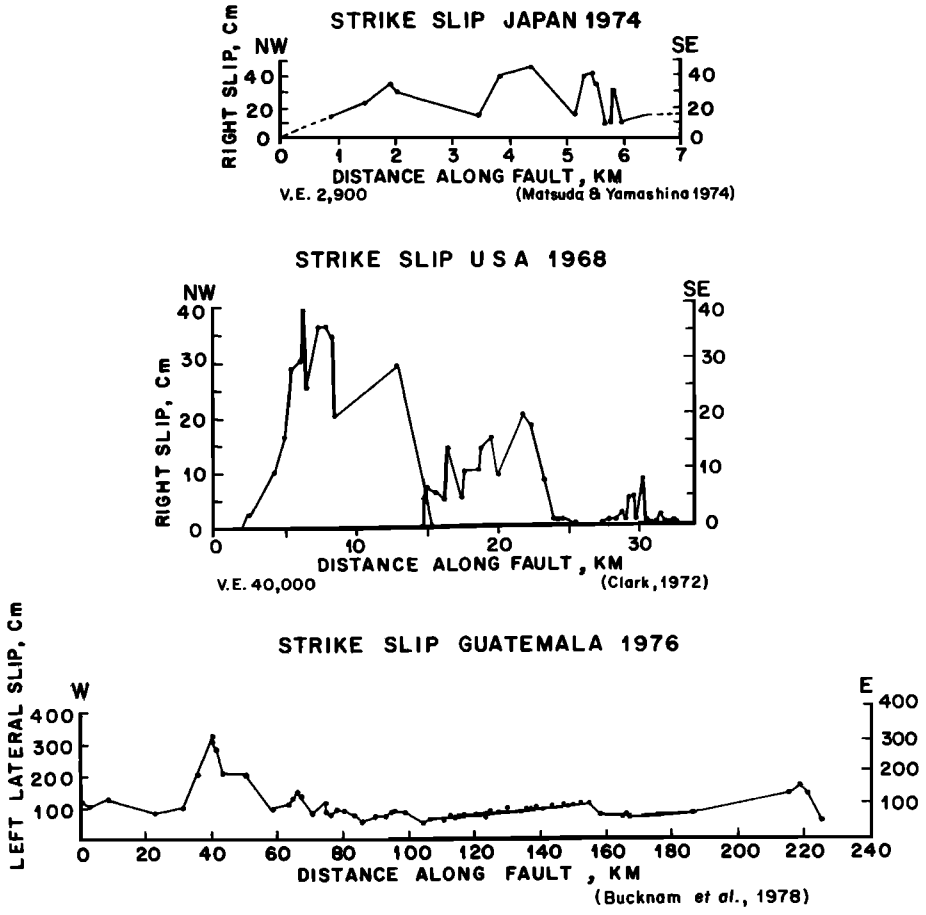

Fig. 15. Irregularity in observed surface static displacements following three major earthquakes.

Acknowledgments. The authors gratefully acknowledge Peter Worcester who loaned us the transient recorders, interfaces, and tape drives, without which these experiments could not have been performed. The authors also wish to thank Ralph Lovberg, who first suggested the use of photosensitive field effect transistors. The authors benefited from numerous discussions with James N. Brune. The authors are indebted to Mark Hernandez for his electronic expertise in the development and building of the Fotofet circuitry. This research was supported in part by National Science Foundation grant AEN74-13264 and is a contribution of the Scripps Institution of Oceanography.

References

Archuleta, R. J., and J. N. Brune, Surface strong motion associated with a stick-slip event in a foam rubber model of earthquakes, Bull. Seismol. Soc. Amer., 65, 1059-1071, 1975.

Archuleta, R. J., and G. A. Frazier, Three-dimensional numerical simulations of dynamic faulting in a half-space, Bull. Seismol. Soc. Amer., 68, 541-572, 1978.

Boore, D. M., and W. B. Joyner, The influence of rupture incoherence on seismic directivity, Bull. Seismol. Soc. Amer., 68, 283-300, 1978.

Brune, J. N., Tectonic stress and the spectra of seismic shear waves from earthquakes, J. Geophys. Res., 75, 4997-5009, 1970.

Brune, J. N., Earthquake modeling by stick-slip along precut surfaces in stressed foam rubber, Bull. Seismol. Soc. Amer., 63, 2105-2119, 1973.

Bucknam, R. C., G. Plafker, and R. V. Sharp, Fault movement (afterslip) following the Guatemala earthquake of February 4, 1976, Geology, 6, 170-173, 1978.

Burford, R. O., Continued slip on the Coyote Creek fault after the Borrego Mountain earthquake, in the Borrego Mountain earthquake of April 9, 1968, U.S. Geol. Surv. Prof. Pap., 787, 105-111, 1972.

Clark, M., Surface rupture along the Coyote Creek fault, the Borrego Mountain earthquake of April 9, 1968, U.S. Geol. Surv. Prof. Pap., 787, 55-87, 1972.

Eshelby, J. D., The determination of the elastic field of an ellipsoidal inclusion, and related problems, Proc. Roy. Soc. London, 241, 376-396, 1957.

Geller, R. J., Scaling relations for earthquake source parameters and magnitudes, Bull. Seismol. Soc. Amer., 66, 1501-1523, 1976.

Hanson, M. E., A. R. Sanford, and R. J. Shaffer, A source function for a dynamic brittle unilateral shear fracture, Geophys. J. Roy. Astron. Soc., 38, 365-376, 1974.

Hartzell, S. H., and J. N. Brune, Source parameters for the January 1975 Brawley-Imperial Valley earthquake swarm, Pure Appl. Geophys., 115, 333-355, 1977.

Hartzell, S. H., G. A. Frazier, and J. N. Brune,

Earthquake modeling in a homogeneous half-space, Bull. Seismol. Soc. Amer., 68, 301-316, 1978.

Kanamori, H., Determination of effective tectonic stress associated with earthquake faulting. The Tottori earthquake of 1943, Phys. Earth Planet. Interiors, 5, 426-434, 1972.

Kanamori, H., Mode of strain release associated with major earthquakes in Japan, Annu. Rev. Earth Planet. Sci., 1, 213-239, 1973.

Kanamori, H., and G. Stewart, Seismological aspects of the Guatemala earthquake of February 4, 1976, J. Geophys. Res., 83, 3427-3434, 1978.

Keilis-Borok, V. I., On estimation of the displacement in an earthquake source and of source dimensions, Ann. Geofis., 12, 205-214, 1959.

Knopoff, L., Energy release in earthquakes, Geophys. J. Roy. Astron. Soc., 1, 44-52, 1958.

Matsuda, T., and K. Yamashina, Surface faults associated with the Izu-Hanto-Oki earthquake of 1974, Japan, Preliminary report on the Izu-Hanto-Oki earthquake of 1974, Bull. Earthquake Res. Inst. Tokyo Univ., 14, 135-158, 1974.

Neuber, H., Theory of notch stresses: Principles for exact calculation of strength with reference to structural form and material, in Kerbspannungslehre, Springs, Berlin, 1937. (English translation, AEC-tr-4547, The Office of Technical Information, Arlington, VA., 1958.)

Nur, A., Nonuniform friction as a physical basis for earthquake mechanics: A review, in Proceedings of Conference II on Experimental Studies of Rock Friction With Application to Earthquake Prediction, pp. 241-288, U.S. Geological Survey, Menlo Park, CA, 1977.

Richards, P. G., The dynamic field of a growing plane elliptical shear crack, Int. J. Solids Structures, 9, 843-861, 1973.

Smith, S. W., and M. Wyss, Displacement on the San Andreas fault subsequent to the 1966 Parkfield earthquake, Bull. Seismol. Soc. Amer., 58, 1955-1973, 1968.

(Received August 23, 1978;
revised January 31, 1979;
accepted February 2, 1979.)